
Article:
Shukhobodskaia, D. and Erdelyi, R. (2018) Propagation of Surface Magnetohydrodynamic Waves in Asymmetric Multilayered Plasma. The Astrophysical Journal, 868 (2). 128. ISSN 0004-637X

https://doi.org/10.3847/1538-4357/aae83c

The Astrophysical Journal, 868:128 (16pp), 2018 December 1 https://doi.org/10.3847/1538-4357/aae83c

Propagation of Surface Magnetohydrodynamic Waves in Asymmetric Multilayered Plasma

Daria Shukhobodskaia[1] and Róbert Erdélyi[1,2]
[1] Solar Physics and Space Plasma Research Centre, School of Mathematics and Statistics, University of Sheffield, Hicks Building, Hounsfield Road, Sheffield, S3 7RH, UK; robertus@sheffield.ac.uk
[2] Department of Astronomy, Eötvös Loránd University, Pázmány Péter sétány 1/A, H-1117 Budapest, Hungary
Received 2018 May 10; revised 2018 October 12; accepted 2018 October 12; published 2018 November 30

Abstract

Investigation of magnetohydrodynamic wave propagation in different equilibrium configurations is important for the development of solar magnetoseismology. In the present work, a magnetized plasma slab sandwiched between an arbitrary number of nonmagnetic layers is considered and an analytical approach is used for the derivation of its dispersion relation. This work is a natural generalization of the symmetric slab model studied by Roberts and the asymmetric magnetic slab model, considered by Allcock & Erdélyi. Similar to the dispersion relation for an asymmetric slab, and unlike a symmetric slab, the dispersion relation for an asymmetric multilayered plasma cannot be decoupled into sausage and kink eigenmodes. The waves that permitted us to propagate in multilayered slabs have mixed characters; therefore, the notion of quasi-sausage and quasi-kink waves is more appropriate. Here, we focus on how a multilayered structuring affects the eigenmodes. The amplitudes of the eigenmodes depend on the equilibrium structuring and the model parameters; this motivates an application as a solar magnetoseismology tool. Finally, specific cases of two- and three-layered slabs are studied in detail and their potential applicability to magnetic bright points is discussed.

Key words: magnetohydrodynamics (MHD) – Sun: corona – Sun: magnetic fields – Sun: oscillations – Sun: photosphere – waves

1. Introduction

The solar atmosphere, from the photosphere to the corona, is dominated by a complex and dynamic magnetic field that makes the plasma highly structured. Multiwavelength observations from high-resolution satellites and ground-based telescopes enable the detection of periodic motions in different magnetic structures in the solar atmosphere, such as in coronal loops (Thompson et al. 1998; Wang 2004; Aschwanden 2005; Banerjee et al. 2007; De Moortel 2009), plumes (Ofman et al. 1997; DeForest & Gurman 1998; Nakariakov 2006), prominences (Arregui et al. 2012), solar wind (Belcher 1971; Abbo et al. 2016), and spicules (Zaqarashvili & Erdélyi 2009; Tsiropoula et al. 2012).

These observed periodic perturbations may be described in terms of magnetohydrodynamic (MHD) waves. They provide us with a tool to diagnose these structures, a method known as solar magnetoseismology (SMS; see reviews by Nakariakov & Verwichte 2005; Erdélyi 2006a, 2006b; Andries et al. 2009; Ruderman & Erdélyi 2009). High-resolution observations of waves and oscillations in magnetic structures, combined with theoretical MHD wave modeling, enable us to determine solar atmospheric parameters that are difficult to measure directly, such as the coronal magnetic field strength (Nakariakov & Ofman 2001; Erdélyi & Taroyan 2008). The principles of SMS were first suggested by Uchida (1970), Zaitsev & Stepanov (1975), and Roberts et al. (1984) for coronal application, and by Tandberg-Hanssen (1995) for prominence application.

MHD wave propagation is a popular topic with plenty of applications to solar and solar-terrestrial plasmas. Their significance has increased not only because of their potential as a remote diagnostic tool, as outlined above, but also due to their presumed contribution to plasma heating processes. It is believed that the heating processes that generate and sustain the hot solar atmosphere may be accounted for by the MHD waves (Alfvén 1947; Osterbrock 1961; Ionson 1978; Hollweg 1991; Goossens et al. 2011; Mathioudakis et al. 2013) that are generated by the convection reservoir and propagating from the lower atmosphere (Roberts 2000).

Many MHD wave models employ slab geometry where a magnetic slab is embedded in an (a)symmetric, semi-infinite, (non)magnetic environment, e.g. Roberts (1981a, 1981b), Edwin & Roberts (1982), Allcock & Erdélyi (2017), and Zsámberger et al. (2018). Cylindrical geometry is often better for modeling magnetic structures in the corona, whereas slab geometry appears to be a reasonable representation of structures closer to the photosphere, such as magnetic bright points (MBPs), sunspot light bridges, or light walls (Yuan et al. 2014; Yang et al. 2016, 2017). MBPs are small-scale magnetic elements between granular cells of different temperatures and densities.

However, real plasma structuring is more complicated than a simple slab model. A more realistic model, with a number of applications, is a plasma structured by a finite number of parallel discontinuities, which was studied in the incompressible limit by Ruderman (1992). Another model is a magnetized plasma slab sandwiched between an arbitrary number of interfaces with different densities and temperatures with a straight and uniform magnetic field only present in one layer. We consider the existence of MHD waves in this model in the present work. The general dispersion relation is derived and is solved analytically for the cases of two (i.e. one magnetic and one nonmagnetic) or three (i.e., a magnetic slab sandwiched between two asymmetric) slabs in the cases of an incompressible fluid and under the thin-slab approximation.

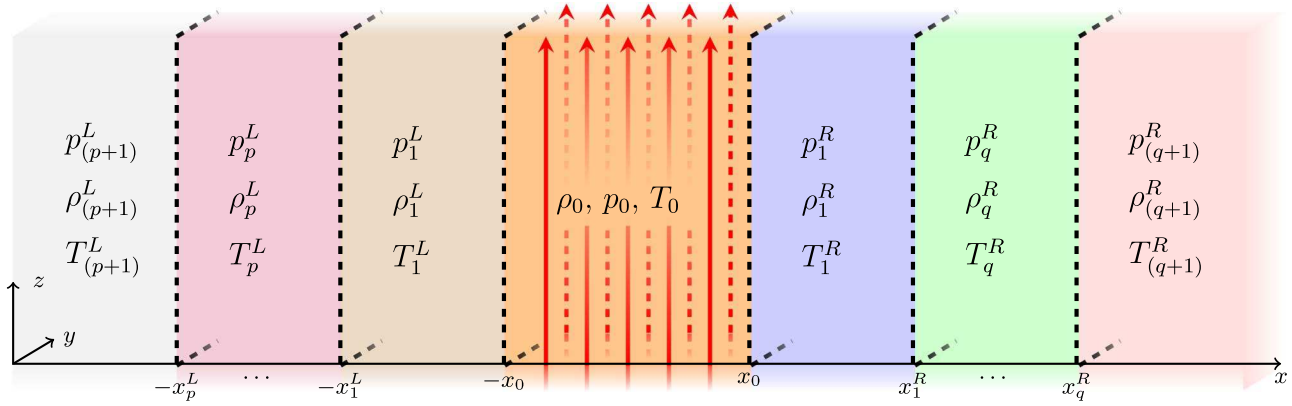

Figure 1. Equilibrium configuration of a layered plasma. The red arrows represent the vertical magnetic field, $B(x)\hat{z}$. Kinetic pressure, $p_i^{L/R}$, density, $\rho_i^{L/R}$, and temperature, $T_i^{L/R}$, are equilibrium parameters. The subscript i corresponds to the relevant slab and varies from 1 to $p+1$ on the left side and from 1 to $q+1$ on the right side, where L/R corresponds to left/right.

2. Derivation of General Dispersion Relation

Consider an infinite compressible inviscid static plasma embedded in a uniform and confined region $|x| \leqslant x_0$ with magnetic field $B(x)\,\hat{z}$, where

$$B(x) = \begin{cases} B_0, & |x| \leqslant x_0, \\ 0, & |x| > x_0. \end{cases}$$

The effect of gravity is ignored. Inside the magnetic slab, the equilibrium kinetic plasma pressure, density, and temperature are denoted by p_0, ρ_0, and T_0, respectively. $p_i^{L/R}$, $\rho_i^{L/R}$, and $T_i^{L/R}$ denote the equilibrium kinetic pressure, density, and temperature inside the $i-$th slab on the left/right of the magnetic region with subscript i that varies from 1 to $p+1$ on the left side and from 1 to $q+1$ on the right (see Figure 1). In total, there are $p+q+3$ regions, of which one has a magnetic field.

The equations that govern the perturbations within the magnetic slab are the ideal MHD equations:

$$\begin{aligned} \rho\frac{D\boldsymbol{v}}{Dt} &= -\nabla p - \frac{1}{\mu_0}\boldsymbol{B}\times(\nabla\times\boldsymbol{B}), \\ \frac{\partial\rho}{\partial t} &+ \nabla\cdot(\rho\boldsymbol{v}) = 0, \\ \frac{D}{Dt}\left(\frac{p}{\rho^\gamma}\right) &= 0, \\ \frac{\partial\boldsymbol{B}}{\partial t} &= \nabla\times(\boldsymbol{v}\times\boldsymbol{B}), \end{aligned} \tag{1}$$

where μ_0 is the magnetic permeability of free space, γ is the adiabatic index, variables $\boldsymbol{v} = (v_x,\ v_y,\ v_z)$, $\boldsymbol{B}$, p, and ρ are velocity, magnetic field, kinetic pressure, and density, at time t. After linearizing and some algebra, we have

$$\begin{aligned} \left(\frac{\partial}{\partial t^2} - v_A^2\frac{\partial}{\partial z^2}\right)v_x &= \frac{\partial}{\partial x}\left((c_0^2+v_A^2)\nabla\cdot\boldsymbol{v} - v_A^2\frac{\partial v_z}{\partial z}\right), \\ \left(\frac{\partial}{\partial t^2} - v_A^2\frac{\partial}{\partial z^2}\right)v_y &= \frac{\partial}{\partial y}\left((c_0^2+v_A^2)\nabla\cdot\boldsymbol{v} - v_A^2\frac{\partial v_z}{\partial z}\right), \\ \frac{\partial^2 v_z}{\partial t^2} &= c_0^2\frac{\partial}{\partial z}\nabla\cdot\boldsymbol{v}. \end{aligned} \tag{2}$$

Here, $v_A = B_0/\sqrt{\mu_0\rho_0}$ is the Alfvén speed and $c_0 = \sqrt{\gamma p_0/\rho_0}$ is the sound speed in the magnetic slab. The sound speed in the $i-$th left/right nonmagnetic region is denoted by $c_i^{L/R} = \sqrt{\gamma p_i^{L/R}/\rho_i^{L/R}}$. The equilibrium pressure balance across each interface is required, i.e.,

$$\begin{aligned} p^L_{(p+1)} = p^L_p \ &= \ \ldots \ = p^L_1 = p_0 + \frac{B_0^2}{2\mu_0} \\ &= \ p^R_1 \ = \ \ldots \ = p^R_q = p^R_{(q+1)}. \end{aligned} \tag{3}$$

Equation (3) yields to the following relation between characteristic speeds and density ratios for any two nonmagnetic regions:

$$\frac{(c_i^{L/R})^2}{(c_j^{L/R})^2} = \frac{\rho_j^{L/R}}{\rho_i^{L/R}}.$$

We seek a solution to Equations (2) of the following form:

$$\begin{aligned} v_x(\boldsymbol{x},\,t) &= \hat{v}_x(x)e^{i(kz-\omega t)},\ v_y(\boldsymbol{x},\,t) = 0, \\ v_z(\boldsymbol{x},\,t) &= \hat{v}_z(x)e^{i(kz-\omega t)}, \end{aligned} \tag{4}$$

representing wave propagation in the $\hat{z}-$ direction, where ω is the angular frequency and k is the length of the wavenumber vector in the $\hat{z}$-direction. We only consider field-aligned propagation of the perturbations. Substituting solutions (4) into the system of Equations (2), and combining the obtained equations, it is possible to derive an ordinary differential equation for $\hat{v}_x$ representing transversal motions inside the magnetic slab, i.e., $|x| \leqslant x_0$:

$$\frac{d^2\hat{v}_x}{dx^2} - m_0^2\hat{v}_x = 0, \tag{5}$$

where

$$m_0^2 = \frac{(k^2v_A^2-\omega^2)(k^2c_0^2-\omega^2)}{(c_0^2+v_A^2)(k^2c_T^2-\omega^2)}, \quad c_T^2 = \frac{c_0^2v_A^2}{c_0^2+v_A^2}. \tag{6}$$

Note that since $\boldsymbol{k} = (0,\,0,\,k)$, and the system is homogeneous in the $y-$direction, the other transversal component of the motion (i.e., $\hat{v}_y$) representing Alfvén waves decouples. For each of the

left/right nonmagnetic regions, we obtain

$$\frac{d^2\hat{v}_x}{dx^2} - (m_i^{L/R})^2\hat{v}_x = 0, \tag{7}$$

with

$$(m_i^{L/R})^2 = k^2 - \frac{\omega^2}{(c_i^{L/R})^2}. \tag{8}$$

Equations (5) and (7) are formally identical to the corresponding equations for the symmetric slab, considered by Roberts (1981b), if $p = q = 0$ and $\rho_1^L = \rho_1^R = \rho_e$.

Let us assume that the perturbations vanish at infinity so that $\hat{v}_x \to 0$ as $x \to \pm\infty$. It should be noted that m_0^2 and $(m_i^{L/R})^2$ may be positive or negative for i from 1 to p on the left side and from 1 to q on the right side. Taking into account that the wave amplitudes decay exponentially in the ambient, i.e., we are only dealing with trapped waves, we acquire a general solution of Equations (5) and (7) given by

$$\hat{v}_x(x) = \begin{cases} A_{p+1}^L(\cosh m_{p+1}^L x + \sinh m_{p+1}^L x), & \text{for } x < -x_p^L, \\ A_p^L \cosh m_p^L x + B_p^L \sinh m_p^L x, & \text{for } -x_p^L < x < -x_{p-1}^L, \\ \cdots \\ A_1^L \cosh m_1^L x + B_1^L \sinh m_1^L x, & \text{for } -x_1^L < x < -x_0, \\ A_0 \cosh m_0 x + B_0 \sinh m_0 x, & \text{for } |x| \leqslant x_0, \\ A_1^R \cosh m_1^R x + B_1^R \sinh m_1^R x, & \text{for } x_0 < x < x_1^R, \\ \cdots \\ A_q^R \cosh m_q^R x + B_q^R \sinh m_q^R x, & \text{for } x_{q-1}^R < x < x_q^R, \\ A_{q+1}^R(\cosh m_{q+1}^R x - \sinh m_{q+1}^R x), & \text{for } x > x_q^R, \end{cases} \tag{9}$$

where A_i^L, B_j^L, A_s^R, B_t^R, A_0, and B_0, are constants with $i = 1, 2, \ldots p + 1, j = 1, 2, \ldots p, s = 1, 2, \ldots q + 1$ and $t = 1, 2, \ldots q$. The total (kinetic plus magnetic) pressure perturbation, $P_T(\boldsymbol{x}, t)$, satisfies the equation

$$\frac{\partial P_T}{\partial t} = \rho_0 v_A^2 \frac{\partial v_z}{\partial z} - \rho_0(c_0^2 + v_A^2)\nabla \cdot \boldsymbol{v}. \tag{10}$$

Considering $P_T(\boldsymbol{x}, t)$ in a Fourier form, $P_T(\boldsymbol{x}, t) = \hat{p}\,(x)e^{i(kz-\omega t)}$, and employing Equations (2) and (10), we obtain that

$$\hat{p}\,(x) = \hat{v}_x{}'(x)\begin{cases} \Lambda_{p+1}^L/m_{p+1}^L, & \text{for } x < -x_p^L, \\ \Lambda_p^L/m_p^L, & \text{for } -x_p^L < x < -x_{p-1}^L, \\ \cdots \\ \Lambda_1^L/m_1^L, & \text{for } -x_1 < x < -x_0, \\ \Lambda_0/m_0, & \text{for } |x| \leqslant x_0, \\ \Lambda_1^R/m_1^R, & \text{for } x_0 < x < x_1^R, \\ \cdots \\ \Lambda_q^R/m_q^R, & \text{for } x_{q-1}^R < x < x_q^R, \\ \Lambda_{q+1}^R/m_{q+1}^R, & \text{for } x > x_q^R, , \end{cases} \tag{11}$$

where

$$\Lambda_0 = -\frac{i\rho_0(k^2v_A^2 - \omega^2)}{m_0\omega}, \quad \Lambda_j^L = \frac{i\rho_j^L\omega}{m_j^L}, \quad \text{for } j = 1, 2, \ldots\ p + 1, \quad \text{and} \quad \Lambda_l^R = \frac{i\rho_l^R\omega}{m_l^R}, \quad \text{for } l = 1, 2, \ldots\ q + 1. \tag{12}$$

Let us now establish appropriate boundary conditions. For physical solutions, the velocity, $v_x(\boldsymbol{x}, t)$, and total pressure, $P_T(\boldsymbol{x}, t)$, have to be continuous across the boundaries $x = -x_i^L$, $x = \pm x_0$ and $x = x_j^R$, for $i = 1 \ldots p$ and $j = 1 \ldots q$. Equations (9) and (11) give us $4 + 2(p + q)$ coupled homogeneous algebraic equations:

$$\begin{aligned}
&A_{p+1}^L(\cosh m_{p+1}^L x_p^L - \sinh m_{p+1}^L x_p^L) = A_p^L \cosh m_p^L x_p^L - B_p^L \sinh m_p^L x_p^L, \\
&\Lambda_{p+1}^L A_{p+1}^L(\cosh m_{p+1}^L x_p^L - \sinh m_{p+1}^L x_p^L) = \Lambda_p^L(B_p^L \cosh m_p^L x_p^L - A_p^L \sinh m_p^L x_p^L), \\
&A_p^L \cosh m_p^L x_{p-1}^L - B_p^L \sinh m_p^L x_{p-1}^L = A_{p-1}^L \cosh m_{p-1}^L x_{p-1}^L - B_{p-1}^L \sinh m_{p-1}^L x_{p-1}^L, \\
&\Lambda_p^L(B_p^L \cosh m_p^L x_{p-1}^L - A_p^L \sinh m_p^L x_{p-1}^L) = \Lambda_{p-1}^L(B_{p-1}^L \cosh m_{p-1}^L x_{p-1}^L - A_{p-1}^L \sinh m_{p-1}^L x_{p-1}^L), \\
&\cdots \\
&A_1^L \cosh m_1^L x_0 - B_1^L \sinh m_1^L x_0 = A_0 \cosh m_0 x_0 - B_0 \sinh m_0 x_0, \\
&\Lambda_1^L(B_1^L \cosh m_1^L x_0 - A_1^L \sinh m_1^L x_0) = \Lambda_0(B_0 \cosh m_0 x_0 - A_0 \sinh m_0 x_0), \\
&A_0 \cosh m_0 x_0 + B_0 \sinh m_0 x_0 = A_1^R \cosh m_1^R x_0 + B_1^R \sinh m_1^R x_0
\end{aligned}$$

$$
\begin{aligned}
&\Lambda_0(A_0 \sinh m_0 x_0 + B_0 \cosh m_0 x_0))\\
&\quad = \Lambda_1^R(A_1^R \sinh m_1^R x_0 + B_1^R \cosh m_1^R x_0),\\
&\quad \cdots\\
&A_{q-1}^R \cosh m_{q-1}^R x_{q-1}^R + B_{q-1}^R \sinh m_{q-1}^R x_{q-1}^R\\
&\quad = A_q^R \cosh m_q^R x_{q-1}^R + B_q^R \sinh m_q^R x_{q-1}^R,\\
&\Lambda_{q-1}^R(A_{q-1}^R \sinh m_{q-1}^R x_{q-1}^R + B_{q-1}^R \cosh m_{q-1}^R x_{q-1}^R)\\
&\quad = \Lambda_q^R(A_q^R \sinh m_q^R x_{q-1}^R + B_q^R \cosh m_q^R x_{q-1}^R),\\
&A_q^R \cosh m_q^R x_q^R + B_q^R \sinh m_q^R x_q^R\\
&\quad = A_{q+1}^R(\cosh m_{q+1}^R x_q^R - \sinh m_{q+1}^R x_q^R),\\
&\Lambda_q^R(A_q^R \sinh m_q^R x_q^R + B_q^R \cosh m_q^R x_q^R)\\
&\quad = \Lambda_{q+1}^R A_{q+1}^R(\sinh m_{q+1}^R x_q^R - \cosh m_{q+1}^R x_q^R). \qquad (13)
\end{aligned}
$$

Here, $A_i^{L/R}$ are constant with respect to x. We now rewrite the above equations into the following compact matrix form:

$$
\begin{aligned}
&\boldsymbol{M}(A_{p+1}^L, A_p^L, B_p^L, \ \ldots\ A_1^L, B_1^L, A_0,\\
&\quad B_0, A_1^R, B_1^R, \ \ldots\ A_q^R, B_q^R, A_{q+1}^R)^T = 0, \qquad (14)
\end{aligned}
$$

where $\boldsymbol{M}$ is a $[4 + 2\ (p + q)] \times [4 + 2\ (p + q)]$ matrix. The precise form of the matrix $\boldsymbol{M}$ is given by Equations (33)–(38)) in Appendix A.

In order to have a nontrivial solution of the system, the determinant of the matrix $\boldsymbol{M}$ must be equal to zero:

$$\det \boldsymbol{M} = 0. \qquad (15)$$

Equation (15) is the dispersion relation of the multilayer system. In general, unlike the symmetric case studied, e.g., by Roberts (1981b), the dispersion relation Equation (15) cannot be decoupled into two equations that correspond to the well-known sausage (oscillations at the slab boundaries in antiphase, that correspond mathematically to the equation containing $\tanh m_0 x_0$) and kink (perturbations of the slab boundaries oscillating in-phase that correspond to the equation with $\coth m_0 x_0$) MHD waves. Solutions to Equation (15) will provide modes modified by the density difference at the sides of the magnetic slab similar to a single asymmetric slab investigated by Allcock & Erdélyi (2017). We adopt the notions of quasi-sausage and quasi-kink to describe these eigenmodes, because they have mixed characters. The slab cross-sectional width, that is constant for symmetric kink modes, is affected for asymmetric kink modes and the line of zero perturbation is shifted for asymmetric sausage modes when compared to the symmetric case, namely, the center of the slab. Furthermore, both the sausage and kink modes can be further categorized as body and surface modes. Surface waves exist when $m_0^2 > 0$, which corresponds to evanescent solutions of Equation (5), while body waves exist when $m_0^2 < 0$, which corresponds to spatially oscillatory solutions. This nomenclature for wave classification was introduced by Roberts (1981b) for symmetric and Allcock & Erdélyi (2017) for asymmetric equilibria.

Let us now consider some specific cases of an asymmetric multilayered plasma slab structure that are analytically solvable and have potential for solar application. First, by setting $p = q = 0$, we verify that the dispersion relation reduces to that which governs the asymmetric slab configuration of Allcock & Erdélyi (2017), namely,

$$\tanh 2m_0 x_0(\Lambda_0\Lambda_0 + \Lambda_1^L\Lambda_1^R) + \Lambda_0(\Lambda_1^L + \Lambda_1^R) = 0. \qquad (16)$$

We will now focus on cases of two layers (one magnetic and one nonmagnetic), and three (a magnetic layer sandwiched between two nonmagnetic) slabs, respectively, and investigate how the multilayered structure affects the eigenmodes and their eigenfunctions.

2.1 Two-slab Case

Let us first consider the case of two slabs, represented by $p = 1$ and $q = 0$, which is illustrated by Figure 2. The width of the nonmagnetic and magnetic slabs are denoted as d_1^L and d_0, respectively. Such a model could be useful for modeling MHD waves in MBPs of the solar photosphere (as shown on Figure 3). MBPs are approximately vertical magnetic structures between supergranule convection cells of different densities and temperatures. Since neighboring granular cells affect the MBP, we can apply a two-slab description to analyze what will change when comparing eigenmodes to MHD waves in a single slab case.

From condition (15), we obtain the dispersion relation

$$
\begin{aligned}
&\tanh 2m_0 x_0[\Lambda_0\Lambda_0(\Lambda_1^L - \Lambda_2^L \tanh m_1^L(x_0 - x_1^L))\\
&\quad + \Lambda_1^L\Lambda_1^R(\Lambda_2^L - \Lambda_1^L \tanh m_1^L(x_0 - x_1^L))]\\
&\quad + \Lambda_0[\Lambda_1^L(\Lambda_1^R + \Lambda_2^L) - (\Lambda_1^L\Lambda_1^L + \Lambda_1^R\Lambda_2^L)\\
&\quad \times \tanh m_1^L(x_0 - x_1^L)] = 0. \qquad (17)
\end{aligned}
$$

Note, that the two-slab case may be reduced to the single slab case, by letting $x_0 = x_1^L$ and $\Lambda_1^L = \Lambda_2^L$. By substituting notations introduced by Equation (12) into the dispersion relation (17), we obtain

$$
\begin{aligned}
&\tanh 2m_0 x_0\Bigg[\omega^4 \frac{m_0^2}{\rho_0^2} + \frac{m_1^R}{\rho_1^R}\frac{m_2^L}{\rho_2^L}(k^2 v_A^2 - \omega^2)^2\\
&\quad - \left(\frac{m_1^L}{\rho_1^L}\frac{m_1^R}{\rho_1^R}(k^2 v_A^2 - \omega^2)^2 + \frac{m_0^2}{\rho_0^2}\omega^4 \frac{\rho_1^L}{m_1^L}\frac{m_2^L}{\rho_2^L}\right)\\
&\quad \times \tanh m_1^L(x_0 - x_1^L)] - \frac{m_0}{\rho_0}\omega^2(k^2 v_A^2 - \omega^2)\\
&\quad \times \left(\frac{m_1^R}{\rho_1^R} + \frac{m_2^L}{\rho_2^L} - \left(\frac{m_1^R}{\rho_1^R}\frac{m_2^L}{\rho_2^L}\frac{\rho_1^L}{m_1^L} + \frac{m_1^L}{\rho_1^L}\right)\right.\\
&\quad \times \tanh m_1^L(x_0 - x_1^L)) = 0. \qquad (18)
\end{aligned}
$$

Equation (18) is the dispersion relation describing the propagation of quasi-kink and quasi-sausage waves for the case of two (one magnetic and one nonmagnetic) slabs.

Next, let us plot the eigenfunctions using numerical solutions. In Figure 4(a), the effect of varying the density ratios ρ_1^L/ρ_0 and ρ_2^L/ρ_1^L is shown, and its cross-cut slice is plotted in Figure 4(b) for a characteristic value of the ratio $\rho_2^L/\rho_0 = 0.3$. The panels of Figure 4(c) illustrate the behavior

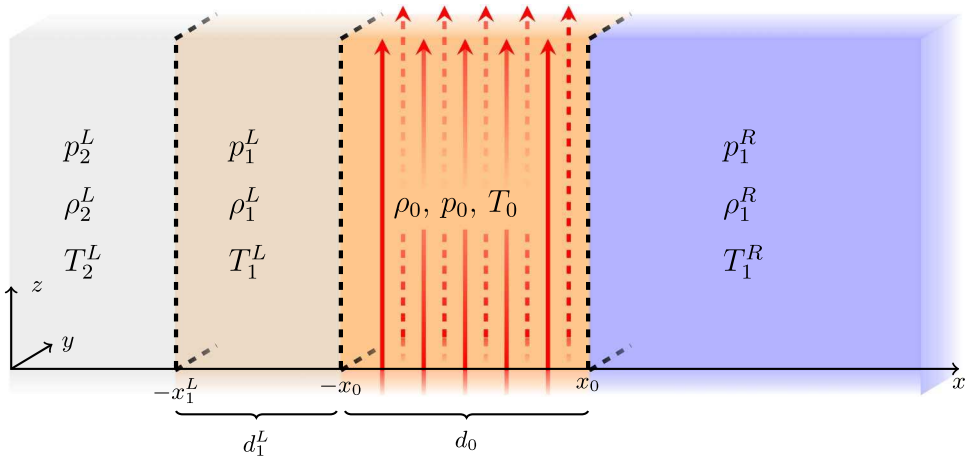

Figure 2. Equilibrium configuration for a two-slab case: a magnetic slab, $|x| \leqslant x_0$, and a nonmagnetic slab, $-x_1^L \leqslant x \leqslant -x_0$.

of slow surface quasi-kink and quasi-sausage modes, in a two-slab system using numerical solutions for the dispersion relation Equation (18) for $\rho_1^L/\rho_0 = 1, 2, 3$. The central plot shows the case where $\rho_1^L = \rho_1^R$. The density ratio is $\rho_1^R/\rho_0 = 2$, the characteristic speed orderings are $c_1^R = 0.7c_0$, $v_A = 0.4c_0$, the nondimensional width of the magnetic slab is $kx_0 = 1.5$ and the width of the nonmagnetic slab is $x_1^L = 2x_0$.

Two important features are notable when inspecting the eigenfunctions of Figure 4(c). First, although the eigenfunctions themselves are continuous, this is not the case for their derivatives, which are discontinuous at the interfaces. Assuming a suitable spatial resolution of linear perturbations during an observation of structured MHD waveguides, the spatial distribution of the eigenfunctions (say transversal velocity, intensity, or the appropriate component of the magnetic field) could be measured and the above discontinuous feature confirmed. Now, from the measured spatial distribution of these eigenfunctions, one may then determine the details of the structuring of the MHD waveguide by means of SMS.

Second, the amplitudes of the perturbations themselves at the boundaries of an asymmetric structured waveguide will not be symmetric with respect to the center of the magnetic waveguide. This information could also be exploited to determine the equilibrium parameters of the MHD waveguide structure, however, that is beyond the scope of the current paper. For an analog of how the concept works for a single asymmetric waveguide, see Allcock & Erdélyi (2018).

Figures 5(a)–(d) reveal the behavior of the slow surface modes as the nonmagnetic slab density is varied with $kx_0 = 0.01$, 0.1, 1, and 3. For a wide slab width $kx_0 \gg 1$, the phenomenon of avoided crossing is visualized in Figure 5(d), i.e., the loci of the eigenvalues of the slow surface modes do not intersect, which demonstrates why the dispersion relation Equation (18) does not decouple into two equations for sausage and kink modes, as it does in the symmetric case. For more on the meaning of avoided crossings of eigenmodes in the present context, see Allcock & Erdélyi (2017). The density ratios are fixed at $\rho_2^L/\rho_0 = 0.3$, $\rho_1^R/\rho_0 = 2$, the characteristic speed orderings are $c_1^R = 0.7c_0$, $v_A = 0.4c_0$ and the width of the nonmagnetic slab is $x_1^L = 2x_0$.

In Figure 6(a), the effect of varying the nondimensional magnetic slab width kx_0 and the ratio d_1^L/d_0 is illustrated. For a characteristic value of the ratio of nonmagnetic slab width to magnetic slab width $d_1^L/d_0 = 0.5$, a cross-cut of Figure 6(a) is plotted in Figure 6(b), and for a specific value of nondimensional magnetic slab $kx_0 = 1.5$ in Figure 7(a). The panels in Figures 6(c) and 7(b) show the slow surface quasi-sausage and quasi-kink modes for different values of the nondimensional magnetic slab width $kx_0 = 0.5$, 1.2, 1.9 and the ratio $d_1^L/d_0 = 0.1$, 0.8, 1.5, respectively. The density ratios are fixed at $\rho_2^L/\rho_0 = 0.3$, $\rho_1^L/\rho_0 = 3$, and $\rho_1^R/\rho_0 = 2$ and the characteristic speed orderings are $c_1^R = 0.7c_0$ and $v_A = 0.4c_0$.

2.2 Three-slab Case

Let us now move on to study the three-slab case as a generalization of the two-slab configuration, to better model, e.g., MBPs. It could help to understand how consideration of a set of multiple granular cells may influence oscillations in MBPs. The case of three adjacent slabs is established when $p = q = 1$ and is visualized in Figure 8, where the widths of the left nonmagnetic slab and right magnetic slab are denoted by $d_1^{L/R}$ and d_0, respectively. The dispersion relation in this case takes the form:

$$\begin{aligned}
&\tanh 2m_0x_0(\Lambda_0\Lambda_0(\Lambda_1^L - \Lambda_2^L \tanh m_1^L(x_0 - x_1^L))\\
&\quad\times(\Lambda_1^R - \Lambda_2^R \tanh m_1^R(x_0 - x_1^R))\\
&\quad+\Lambda_1^L\Lambda_1^R(\Lambda_2^L - \Lambda_1^L \tanh m_1^L(x_0 - x_1^L))\\
&\quad\times(\Lambda_2^R - \Lambda_1^R \tanh m_1^R(x_0 - x_1^R)))\\
&\quad+\Lambda_0(\Lambda_1^L\Lambda_1^R(\Lambda_2^L + \Lambda_2^R)\\
&\quad-\Lambda_1^L(\Lambda_1^R\Lambda_1^R + \Lambda_2^L\Lambda_2^R)\tanh m_1^R(x_0 - x_1^R)\\
&\quad-\Lambda_1^R(\Lambda_1^L\Lambda_1^L + \Lambda_2^L\Lambda_2^R)\tanh m_1^L(x_0 - x_1^L)\\
&\quad+(\Lambda_1^L\Lambda_1^L\Lambda_2^R + \Lambda_1^R\Lambda_1^R\Lambda_2^L)\\
&\quad\times\tanh m_1^L(x_0 - x_1^L)\tanh m_1^R(x_0 - x_1^R)) = 0. \qquad (19)
\end{aligned}$$

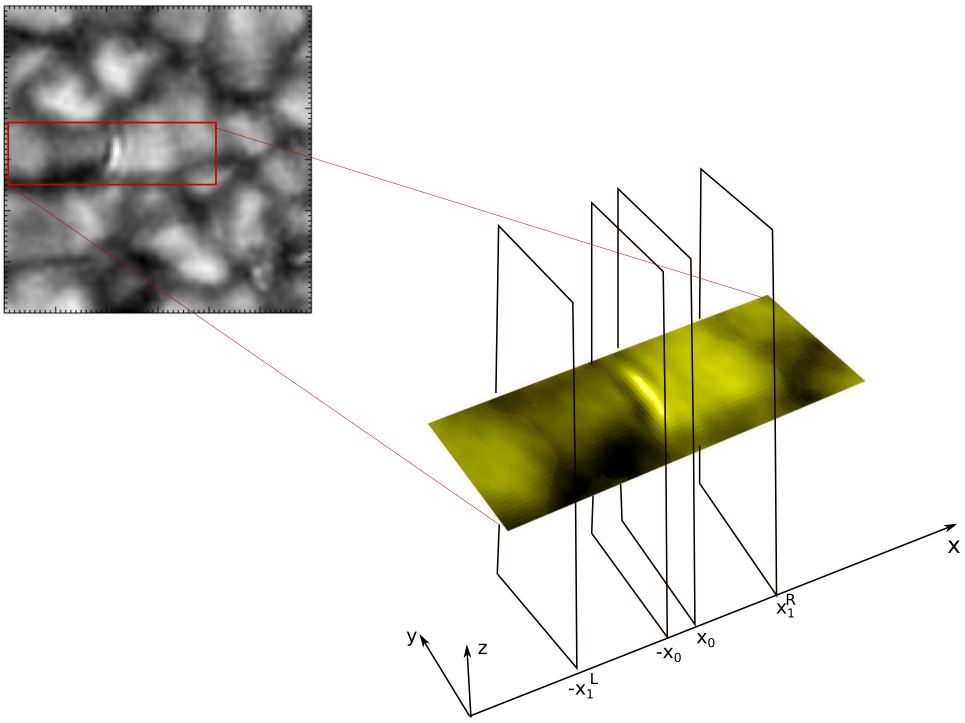

Figure 3. Asymmetric multislab approximation for an elongated MBP, based on Figure 11 of Liu et al. (2018), observed by the New Vacuum Solar Telescope in TiO 7058 Å.

Substituting back the notations of (12), we arrive at

$$\tanh 2m_0x_0\left(\omega^4\frac{m_0^2}{\rho_0^2}\left(\frac{m_1^L}{\rho_1^L}-\frac{m_2^L}{\rho_2^L}\tanh m_1^L(x_0-x_1^L)\right)\right.$$
$$\times\left(\frac{m_1^R}{\rho_1^R}-\frac{m_2^R}{\rho_2^R}\tanh m_1^R(x_0-x_1^R)\right)$$
$$+\frac{m_1^L}{\rho_1^L}\frac{m_1^R}{\rho_1^R}(k^2v_A^2-\omega^2)^2$$
$$\times\left(\frac{m_2^L}{\rho_2^L}-\frac{m_1^L}{\rho_1^L}\tanh m_1^L(x_0-x_1^L)\right)$$
$$\left.\times\left(\frac{m_2^R}{\rho_2^R}-\frac{m_1^R}{\rho_1^R}\tanh m_1^R(x_0-x_1^R)\right)\right)$$
$$-\frac{m_0}{\rho_0}\omega^2(k^2v_A^2-\omega^2)\left(\frac{m_1^L}{\rho_1^L}\left(\frac{m_1^R}{\rho_1^R}\frac{m_2^R}{\rho_2^R}+\frac{m_1^R}{\rho_1^R}\frac{m_2^L}{\rho_2^L}\right.\right.$$
$$\left.-\left(\frac{m_2^L}{\rho_2^L}\frac{m_2^R}{\rho_2^R}+\left(\frac{m_1^R}{\rho_1^R}\right)^2\right)\tanh m_1^R(x_0-x_1^R)\right)$$
$$-\tanh m_1^L(x_0-x_1^L)\left(\frac{m_1^R}{\rho_1^R}\left(\frac{m_1^L}{\rho_1^L}\right)^2+\frac{m_1^R}{\rho_1^R}\frac{m_2^L}{\rho_2^L}\frac{m_2^R}{\rho_2^R}\right.$$
$$\left.\left.-\left(\left(\frac{m_1^L}{\rho_1^L}\right)^2\frac{m_2^R}{\rho_2^R}+\left(\frac{m_1^R}{\rho_1^R}\right)^2\frac{m_2^L}{\rho_2^L}\right)\right.$$
$$\left.\times\tanh m_1^R(x_0-x_1^R)\right))=0. \quad (20)$$

Equation (20) is the dispersion relation for the three-slab case with one magnetic slab embedded between two nonmagnetic plasma slabs with different equilibrium parameters. It was shown by Roberts (1981b) that the dispersion relation governing wave propagation in the case of a single symmetric slab consists of two decoupled equations, describing sausage and kink MHD waves. For the two- and three-slab cases, similarly to the one-slab asymmetric case, the dispersion relation is a single equation, which describes the propagation of quasi-kink and quasi-sausage waves.

In the symmetric case, where $\rho_1^L=\rho_1^R=\rho_1$ and $\rho_2^L=\rho_2^R=\rho_2$, the dispersion relation (20) decouples into two equations, one with tanh (sausage mode) and one with coth (kink mode):

$$\frac{\rho_1}{\rho_0}\omega^2m_0(m_1\rho_2-m_2\rho_1\tanh m_1(x_0-x_1))\begin{pmatrix}\tanh m_0\,x_0\\ \coth m_0\,x_0\end{pmatrix}$$
$$=m_1(k^2v_A^2-\omega^2)(m_2\rho_1-m_1\rho_2\tanh m_1(x_0-x_1)). \quad (21)$$

3. Analytical Solutions

Let us now consider the analytical examination of the dispersion relations (18) and (20) under the incompressible and thin-slab approximations.

3.1. Spurious Solutions

It is obvious that $\omega=k^2v_A^2$ is an exact solution of both of the dispersion relations (18) and (20). However, for this solution,

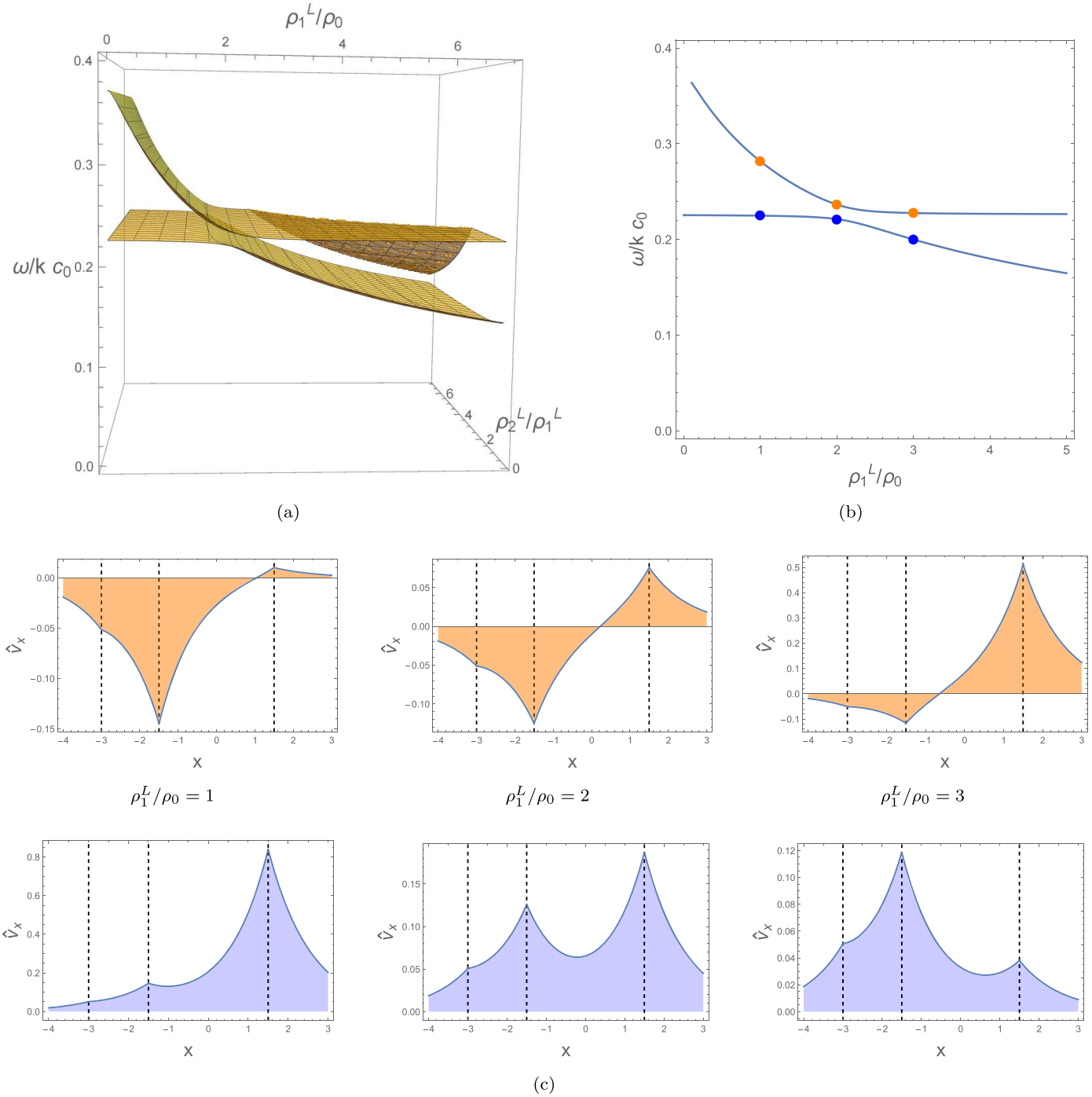

Figure 4. (a) Slow surface mode solutions of the dispersion relation (18) showing the effect of varying the density ratios ρ_1^L/ρ_0 and ρ_2^L/ρ_1^L. Panel (b) is a cross-cut of panel (a) for $\rho_2^L/\rho_0 = 0.3$. Distributions of the transverse velocity perturbation, $\hat{v}_x$, for given density ratios are plotted on panels (c). Here, the other density ratio is fixed at $\rho_1^R/\rho_0 = 2$. The characteristic speed ordering is $c_1^R = 0.7c_0$, $v_A = 0.4c_0$, the width of the nondimensional magnetic slab is $kx_0 = 1.5$, and $x_1^L = 2x_0$. The orange (blue) dots in panel (b) corresponds to the quasi-sausage (quasi-kink) mode. The parameters at each blue and orange dot are used to plot the distribution of the transverse velocity perturbation. The upper (lower) rows in panels (c) correspond to the quasi-sausage (quasi-kink) mode solutions corresponding to density ratios $\rho_1^L/\rho_0 = 1$, 2, and 3.

$m_0 = 0$, which leads to a linear solution of the governing differential Equation (5). Hence, this solution is considered to be spurious. The same is true for the solutions $\omega = kc_0$ and $\omega = kc_T$. So, there are no global modes with a finite wavenumber with phase-speed c_T, c_0, or v_A.

3.2. Incompressible Approximation

Magnetoacoustic modes in the incompressible limit arise only from slow modes in the given equilibrium and choice of field-aligned propagation. In general, it is not possible to solve the dispersion relations (18) and (20) analytically, but the

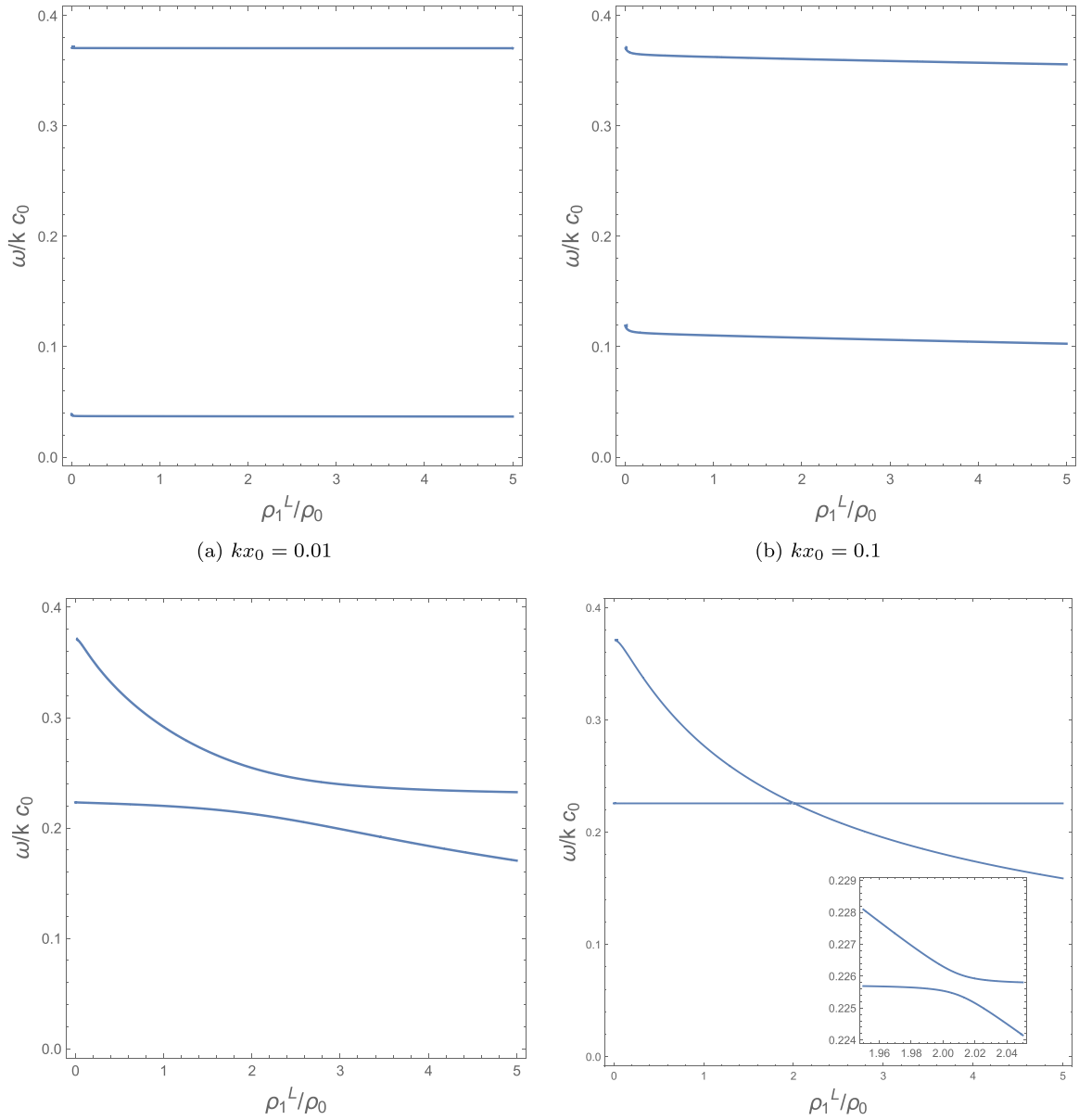

(a) $kx_0 = 0.01$ (b) $kx_0 = 0.1$

(c) $kx_0 = 1$ (d) $kx_0 = 3$

Figure 5. Dependence on the ratio of nonmagnetic slab density to the magnetic slab density is shown in panels (a)–(d) for typical values of nondimensional magnetic slab width $kx_0 = 0.01, 0.1, 1$, and 3. The characteristic speed orderings are $c_1^R = 0.7c_0$ and $v_A = 0.4c_0$, the width of the nonmagnetic slab is $x_1^L = 2x_0$, and the density ratios take values $\rho_2^L/\rho_0 = 0.3$ and $\rho_1^R/\rho_0 = 2$.

incompressible approximation simplifies it significantly and allows us to find an analytical solution. Therefore, we focus on other effects than compressibility. Let us examine the dispersion relations (18) and (20) in the limit $\gamma \to \infty$, where γ is the adiabatic index, corresponding to the approximation of an incompressible plasma. In this limit, we obtain $c_T \to v_A$, hence $m_0 \to k$, $m_i^L \to k$, and $m_j^R \to k$.

3.2.1 Two-slab Case

First, let us study the two-slab case. Here, applying the incompressible approximation, the dispersion relation (18) becomes

$$\tanh 2kx_0\left(\frac{\omega^4}{\rho_0^2}+\frac{(k^2v_A^2-\omega^2)^2}{\rho_1^R\rho_2^L}-\left(\frac{(k^2v_A^2-\omega^2)^2}{\rho_1^L\rho_1^R}+\frac{\omega^4}{\rho_0^2}\frac{\rho_1^L}{\rho_2^L}\right)\tanh k(x_0-x_1^L)\right)-\frac{\omega^2}{\rho_0}(k^2v_A^2-\omega^2)\times\left(\frac{1}{\rho_1^R}+\frac{1}{\rho_2^L}-\left(\frac{\rho_1^L}{\rho_1^R\rho_2^L}+\frac{1}{\rho_1^L}\right)\tanh k(x_0-x_1^L)\right)=0. \quad (22)$$

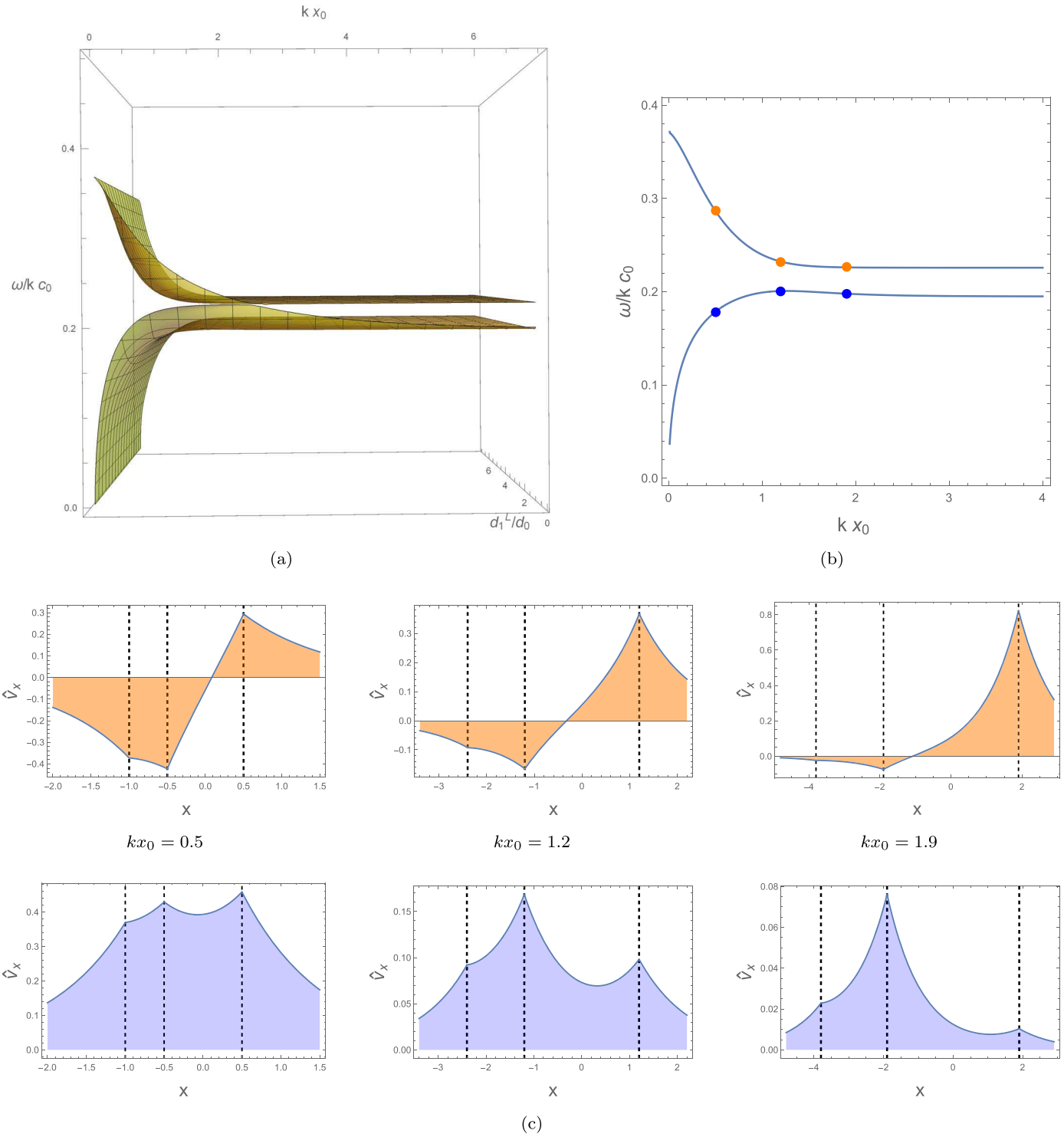

Figure 6. Same as Figure 4, but (a) shows slow surface mode solutions of the dispersion relation (18) emphasizing the effect of varying the ratio of nonmagnetic slab width d_1^L to magnetic slab width d_0. Panel (b) is a cross-cut of panel (a) for $d_1^L/d_0 = 0.5$. In panels (c), distributions of the transverse velocity perturbation $\hat{v}_x$ as the ratio of nondimensional magnetic slab width kx_0 are plotted. The density ratios are fixed at $\rho_1^R/\rho_0 = 2$, $\rho_1^L/\rho_0 = 3$, and $\rho_2^L/\rho_0 = 0.3$. The characteristic speed orderings are $c_1^R = 0.7c_0$ and $v_A = 0.4c_0$, and the nonmagnetic slab width is $x_1^L = 2x_0$.

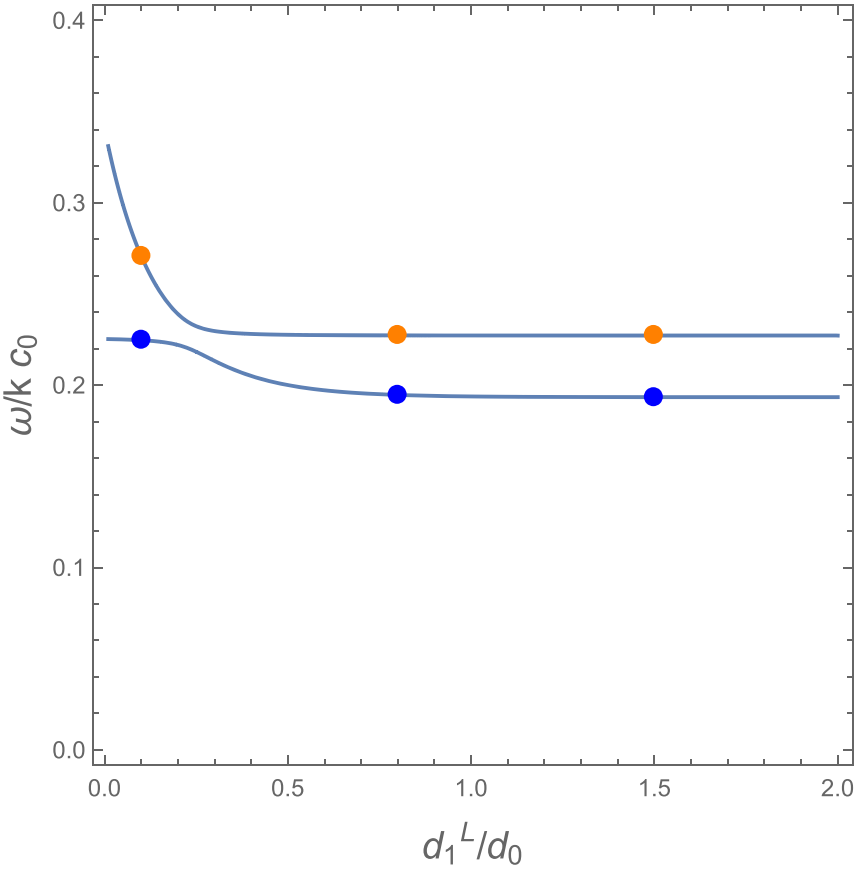

(a)

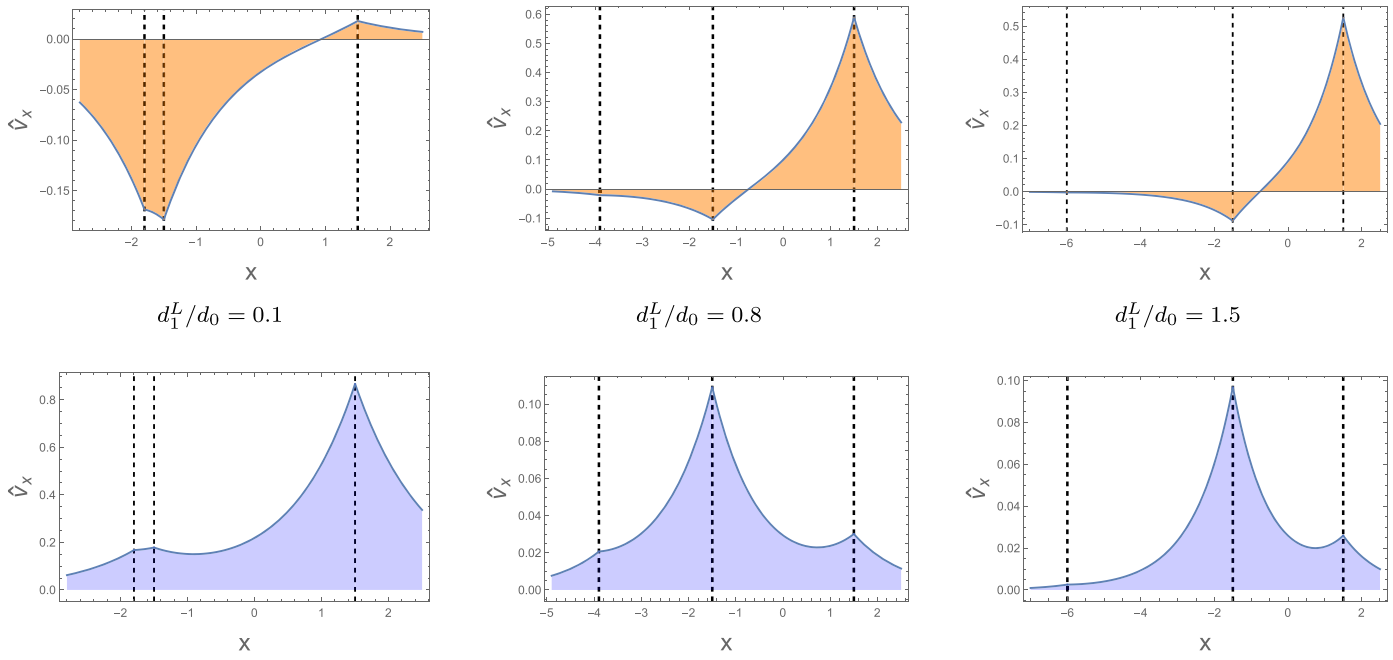

(b)

Figure 7. Same as Figure 4, but the density ratios are now fixed at $\rho_1^R/\rho_0 = 2$, $\rho_1^L/\rho_0 = 3$, and $\rho_2^L/\rho_0 = 0.3$ and nondimensional magnetic slab width is $kx_0 = 1.5$. The characteristic speed orderings are $c_1^R = 0.7c_0$ and $v_A = 0.4c_0$. In panel (b), distributions of the transverse velocity perturbation, $\hat{v}_x$, for a specific value of the ratio of nonmagnetic slab width d_1^L to magnetic slab width d_0 are plotted. The upper (lower) row in panel (b) corresponds to the quasi-sausage (quasi-kink) mode solutions.

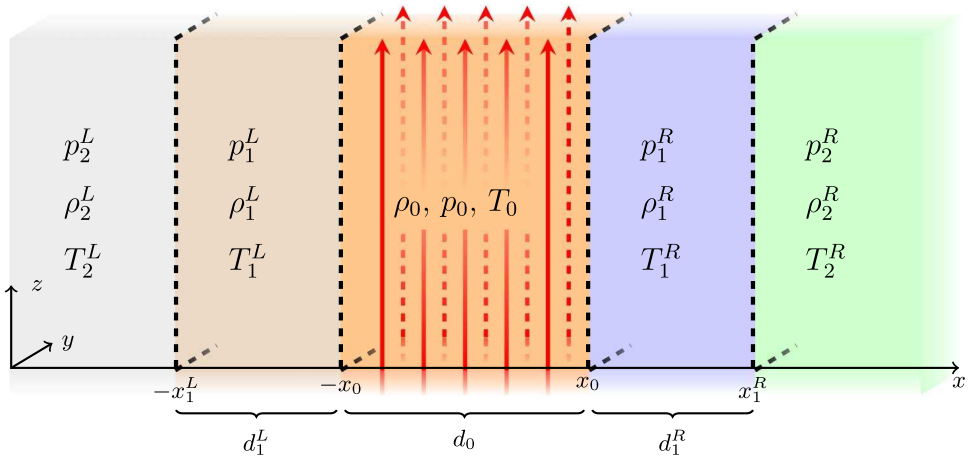

Figure 8. Equilibrium configuration for the three-slab case. A magnetic slab at $|x| \leqslant x_0$ is sandwiched between two nonmagnetic slabs at $-x_1^L \leqslant x \leqslant -x_0$ and $x_0 \leqslant x \leqslant x_1^R$.

Equation (22) is quadratic in ω^2, so we can solve it in a closed form. Its solutions are

$$\omega^2 = \frac{1}{2}k^2 v_A^2 \times \left(\frac{\sigma + 2\rho_0 \coth kx_0 (\rho_1^L - \rho_2^L \tanh k(x_0 - x_1^L)) \pm \sqrt{\varsigma}}{\sigma + 2\frac{\rho_1^L \rho_1^R}{\rho_0} \coth kx_0 (\rho_2^L - \rho_1^L \tanh k(x_0 - x_1^L))} \right), \tag{23}$$

with

$$\begin{aligned} \sigma &= \rho_1^L(\rho_1^R + \rho_2^L + 2\rho_0 \coth kx_0 \\ &+ (\rho_1^R + \rho_2^L)\coth kx_0^2) - (\coth kx_0^2 - 1) \\ &\times ((\rho_1^L \rho_1^L + \rho_1^R \rho_2^L)\cosh 2kx_0 + \rho_0 \rho_2^L \sinh 2kx_0) \\ &\times \tanh k(x_0 - x_1^L),\ \varsigma = (\rho_1^L(\rho_1^R + \rho_2^L) \\ &- (\rho_1^L \rho_1^L + \rho_1^R \rho_2^L)\tanh k(x_0 - x_1^L))^2 (\coth^2 kx_0 - 1)^2 \\ &+ 4\coth^2 kx_0 (\rho_1^L(\rho_1^R - \rho_2^L) \\ &+ (\rho_1^L \rho_1^L - \rho_1^R \rho_2^L)\tanh k(x_0 - x_1^L))^2 . \end{aligned} \tag{24}$$

The solutions given by Equation (23) are surface waves with sub-Alfvénic phase speeds. We introduce the following notation $R_i^{L/R} = \rho_i^{L/R} / \rho_0$.

Figure 9(a) shows the dispersion behavior of two sub-Alfvénic surface modes in one symmetric slab for density ratios $R_2^L = R_1^L = R_1^R = 2$. Figures 9(b)–(d) illustrate that, in the incompressible approximation, the phase speed of the modes approach either the Alfvén speed or zero in the long-wavelength limit. However, when $k \to \infty$, and depending on the external densities, the phase speeds converge to different speeds. Furthermore, when $R_i^L \approx R_i^R$ the converged speeds are almost identical. For Figure 9(b), the density ratios are $R_2^L = 3$, $R_1^L = 1$, and $R_1^R = 2$, for Figure 9(c) density ratios are $R_2^L = 5$, $R_1^L = 10$, and $R_1^R = 0.2$, and in Figure 9(d) $R_2^L = 100$, $R_1^L = 0.1$, and $R_1^R = 0.2$.

3.2.2 Three-slab Case

Similar to the two-slab case, from the dispersion relation (20), we now obtain

$$\begin{aligned} &\tanh 2kx_0 \left(\frac{\omega^4}{\rho_0^2} \left(\frac{1}{\rho_1^L} - \frac{1}{\rho_2^L}\tanh k(x_0 - x_1^L) \right) \right. \\ &\times \left(\frac{1}{\rho_1^R} - \frac{1}{\rho_2^R}\tanh k(x_0 - x_1^R) \right) + \frac{(k^2 v_A^2 - \omega^2)^2}{\rho_1^L \rho_1^R} \\ &\times \left(\frac{1}{\rho_2^L} - \frac{1}{\rho_1^L}\tanh k(x_0 - x_1^L) \right) \\ &\times \left. \left(\frac{1}{\rho_2^R} - \frac{1}{\rho_1^R}\tanh k(x_0 - x_1^R) \right) \right) \\ &- \frac{\omega^2}{\rho_0}(k^2 v_A^2 - \omega^2) \left(\frac{1}{\rho_1^L} \left(\frac{1}{\rho_1^R \rho_2^R} + \frac{1}{\rho_1^R \rho_2^L} \right. \right. \\ &- \left(\frac{1}{\rho_2^L \rho_2^R} + \frac{1}{(\rho_1^R)^2} \right) \\ &\times \tanh k(x_0 - x_1^R)) - \tanh k(x_0 - x_1^L) \\ &\times \left(\frac{1}{\rho_1^R (\rho_1^L)^2} + \frac{1}{\rho_1^R \rho_2^L \rho_2^R} \right. \\ &- \left. \left. \left. \left(\frac{1}{(\rho_1^L)^2 \rho_2^R} + \frac{1}{(\rho_1^R)^2 \rho_2^L}\tanh k(x_0 - x_1^R) \right) \right) \right) \right) = 0. \end{aligned} \tag{25}$$

Equation (25) is quadratic in ω^2 so its analytical solutions exist, namely,

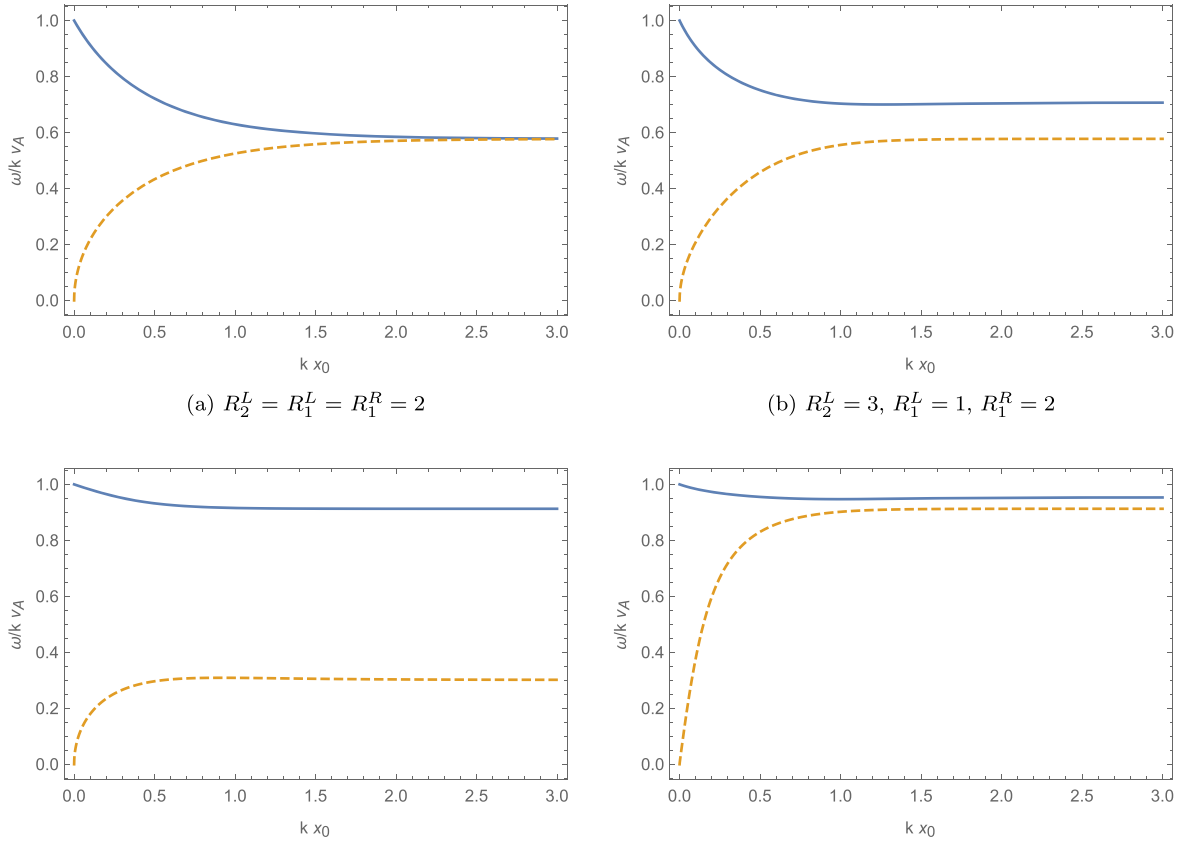

(a) $R_2^L = R_1^L = R_1^R = 2$ (b) $R_2^L = 3,\ R_1^L = 1,\ R_1^R = 2$

(c) $R_2^L = 5,\ R_1^L = 10,\ R_1^R = 0.2$ (d) $R_2^L = 100,\ R_1^L = 0.1,\ R_1^R = 0.2$

Figure 9. Dispersion of MHD modes in an incompressible multilayered symmetric (a) and asymmetric slab (b)–(d) system ($p = 1$, $q = 0$, $x_1^L = 2x_0$). Plotted are the two sub-Alfvénic surface modes for different density ratios $R_i^{L/R} = \rho_i^{L/R}/\rho_0$ for the two-slab case.

$$\omega^2 = \frac{1}{2}k^2 v_A^2 \times \left(\frac{\sigma + \rho_0 \tanh 2kx_0 (\rho_1^L - \rho_2^L \tanh k(x_0 - x_1^L))(\rho_1^R - \rho_2^R \tanh k(x_0 - x_1^R)) \pm \sqrt{\varsigma}}{\sigma + \frac{\rho_1^L \rho_1^R}{\rho_0} \tanh 2kx_0 (\rho_2^L - \rho_1^L \tanh k(x_0 - x_1^L))(\rho_2^R - \rho_1^R \tanh k(x_0 - x_1^R))} \right). \tag{26}$$

Here,

$$\begin{aligned}
\sigma &= \rho_1^L \rho_1^R (\rho_2^L + \rho_2^R + \rho_0 \tanh 2kx_0) \\
&\quad - \rho_1^R (\rho_1^L \rho_1^L + \rho_2^L \rho_2^R + \rho_0 \rho_2^L \tanh 2kx_0) \\
&\quad \times \tanh k(x_0 - x_1^L) - \rho_1^L (\rho_1^R \rho_1^R + \rho_2^L \rho_2^R + \rho_0 \rho_2^R \tanh 2kx_0) \\
&\quad \times \tanh k(x_0 - x_1^R) + (\rho_1^R \rho_1^R \rho_2^L + \rho_1^L \rho_1^L \rho_2^R + \rho_0 \rho_2^L \rho_2^R \\
&\quad \times \tanh 2kx_0) \tanh k(x_0 - x_1^L) \tanh k(x_0 - x_1^R), \\
\varsigma &= -\rho_1^L \rho_1^R (1 - \tanh^2 k(x_0 - x_1^L))(1 - \tanh^2 k(x_0 - x_1^R)) \\
&\quad \times (-2\rho_1^L \rho_2^L \cosh 2k(x_0 - x_1^L) + (\rho_1^L \rho_1^L + \rho_2^L \rho_2^L) \\
&\quad \times \sinh 2k(x_0 - x_1^L))(-2\rho_1^R \rho_2^R \cosh 2k(x_0 - x_1^R) \\
&\quad + (\rho_1^R \rho_1^R + \rho_2^R \rho_2^R) \\
&\quad \times \sinh 2k(x_0 - x_1^R)) \tanh^2 2kx_0 + (-\rho_1^L \rho_1^R (\rho_2^L + \rho_2^R) \\
&\quad + \rho_1^L (\rho_1^R \rho_1^R + \rho_2^L \rho_2^R) \tanh k(x_0 - x_1^R) \\
&\quad + \tanh k(x_0 - x_1^L)(\rho_1^R (\rho_1^L \rho_1^L + \rho_2^L \rho_2^R) \\
&\quad - (\rho_1^R \rho_1^R \rho_2^L + \rho_1^L \rho_1^L \rho_2^R) \tanh k(x_0 - x_1^R)))^2 .
\end{aligned} \tag{27}$$

As well as for the two-slab case, solutions (26) correspond to surface MHD waves with sub-Alfvénic phase speeds. Let us now visualize these solutions. Figure 10(a) illustrates the symmetric case with density ratios $R_2^L = R_2^R = 0.5$ and $R_1^L = R_1^R = 10$. In Figures 10(b)–(d), dispersion is shown under the incompressible approximation, for the case of three adjacent slabs. The behavior of surface modes resembles the two-slab case. Strong dispersion is found for $kx_0 \leqslant 1$, and weak dispersion is found in the short-wavelength limit. In the case of strong asymmetry, Figures 10(c)–(d), the quasi-sausage/kink modes do not seem to converge to the same phase speed. This feature could be exploited for solar magnetoseismology purposes as indication of asymmetric structures. Figure 10(b) corresponds to $R_2^L = 3$, $R_1^L = R_1^R = 2$, and $R_2^R = 0.5$, for Figure 10(c) the density ratios are $R_2^L = 100$, $R_1^L = 70$, $R_1^R = 0.1$, and $R_2^R = 0.5$ and in Figure 10(d) $R_2^L = 0.5$, $R_1^L = 2$, $R_1^R = 10$, and $R_2^R = 1$.

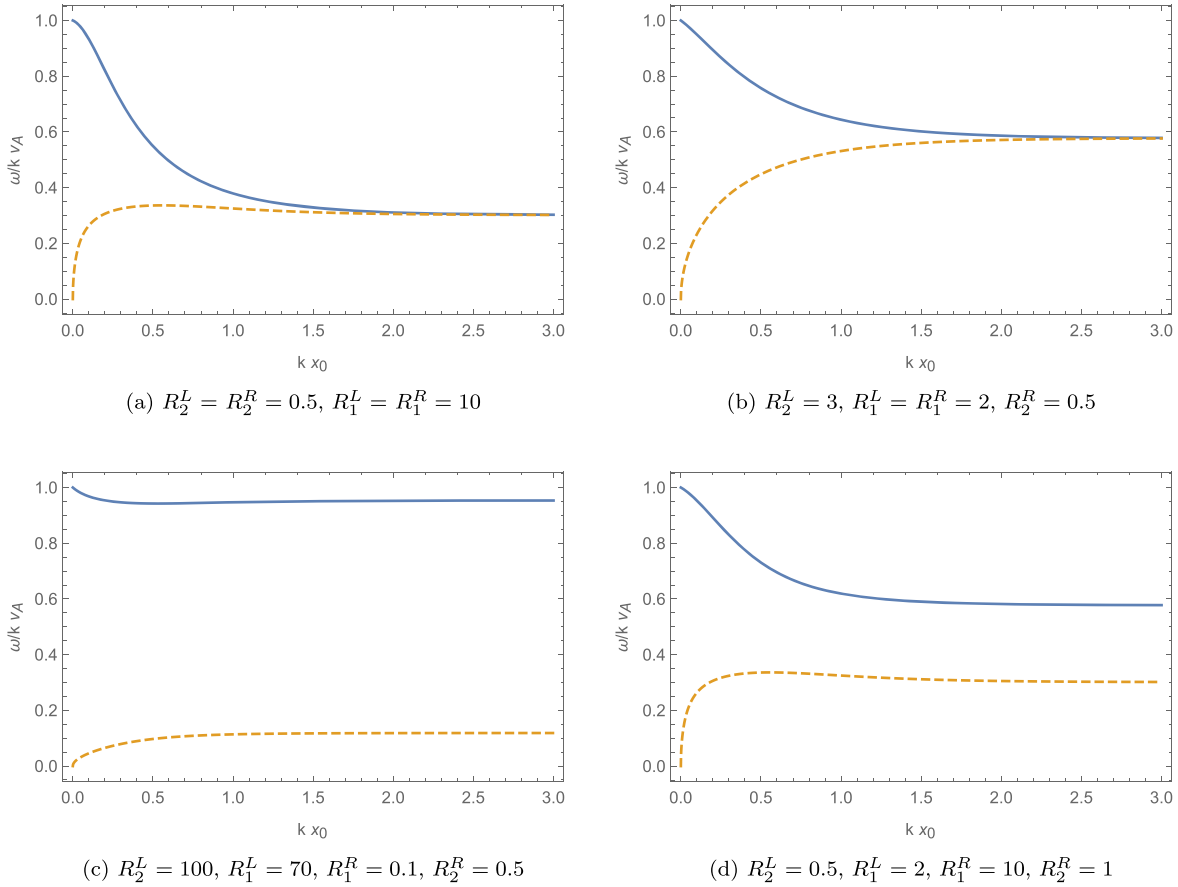

(a) $R_2^L = R_2^R = 0.5$, $R_1^L = R_1^R = 10$

(b) $R_2^L = 3$, $R_1^L = R_1^R = 2$, $R_2^R = 0.5$

(c) $R_2^L = 100$, $R_1^L = 70$, $R_1^R = 0.1$, $R_2^R = 0.5$

(d) $R_2^L = 0.5$, $R_1^L = 2$, $R_1^R = 10$, $R_2^R = 1$

Figure 10. Solutions to the dispersion relation (25) of the modes in an incompressible symmetric (a) and asymmetric (b)–(d) slab for the case of a magnetic slab embedded between two nonmagnetic asymmetric slabs, all in an asymmetric plasma environment, with $p = 1$, $q = 1$, and $x_1^L = x_1^R = 2x_0$.

3.3. Thin-slab Approximation for Surface Waves

By propagating waves in the thin-slab approximation, it is meant the wavelength λ is much greater than the lateral characteristic dimension of the magnetic field. We consider two cases, $d_1^L \approx d_1^R \approx d_0 \ll \lambda$ and $d_1^L \approx d_1^R \ll d_0 \ll \lambda$. The first case corresponds to slabs with similar width, the second one corresponds to a case where the widths of slabs on the left/right are much smaller than that of the central one. We now focus on surface waves, meaning that $m_0^2 > 0$ and $(m_i^{L/R})^2 > 0$. The details of the derivation of the relevant dispersion relation in this approximation are given in Appendix B. Equations (40) and (41) are the dispersion relations for the two-slab case for $d_1^L \approx d_1^R \approx d_0 \ll \lambda$ and $d_1^L \approx d_1^R \ll d_0 \ll \lambda$, respectively. Similarly, Equations (43), (44) correspond to the dispersion relations for the three-slab case under the same assumptions.

3.3.1 Two-slab Case

Let us now investigate the modes in the case of a thin magnetic and nonmagnetic slab embedded in an asymmetric plasma environment. The spurious solution $\omega^2 = k^2 v_A^2$ to Equations (40) and (41) is dealt with in Section 3.1. The other solutions to Equation (41), up to first order in kx_0, are

$$\omega^2 = k^2 c_T^2 \times \left[1 - \frac{2(kx_0)(c_0^2 - c_T^2)}{(c_0^2 + v_A^2)\left(\frac{\rho_0}{\rho_1^R}\sqrt{1 - \frac{c_T^2}{(c_1^R)^2}} + \frac{\rho_0}{\rho_2^L}\sqrt{1 - \frac{c_T^2}{(c_2^L)^2}}\right)}\right], \tag{28}$$

and

$$\omega^2 = k^2 v_A^2 (kx_0) \frac{2\rho_0}{\rho_1^R + \rho_2^L}. \tag{29}$$

Solution (28) behaves like $\omega^2 \to k^2 c_T^2$ as $kx_0 \to 0$. In particular, although there are no modes with a finite wavenumber with phase-speed c_T, there are waves with approximate phase speed c_T that exist only if $c_T < c_1^R$ and $c_T < c_2^L$. This mode is identified as a slow quasi-sausage surface mode. Solution (29) corresponds to the slow quasi-kink surface mode.

3.3.2 Three-slab Case

Let us now analyze the three-slab case in the thin magnetic slab approximation. Similar to the two-slab case, $\omega^2 = k^2 v_A^2$ is a spurious solution to Equations (43) and (44). The slow quasi-sausage surface mode solution to Equation (44) up to first order in kx_0 is

$$\omega^2 = k^2 c_T^2 \left[1 - \frac{2(kx_0)(c_0^2 - c_T^2)}{(c_0^2 + v_A^2)\left(\frac{\rho_0}{\rho_2^R}\sqrt{1 - \frac{c_T^2}{c_{2r}^2}} + \frac{\rho_0}{\rho_2^L}\sqrt{1 - \frac{c_T^2}{c_{2l}^2}}\right)}\right], \tag{30}$$

and the slow quasi-kink surface mode solution is

$$\omega^2 = k^2 v_A^2 (kx_0)\frac{2\rho_0}{\rho_2^R + \rho_2^L}. \tag{31}$$

If $c_{1l} = c_{1r} = c_{2l} = c_{2r} = c_e$ and, hence, $\rho_1^R = \rho_1^L = \rho_2^R = \rho_2^L = \rho_e$, we have one more solution of Equations (41) and (44):

$$\omega^2 = k^2 c_e^2 \left(1 - \left[\frac{(kx_0)\rho_e c_e^2 (c_0^2 - c_e^2)}{\rho_0 (c_0^2 + v_A^2)(c_T^2 - c_e^2)}\right]^2\right). \tag{32}$$

Equation (32) is a quasi-sausage mode. Since the results (28)–(32) do not depend on d_1^L and d_1^R, the results are the same for both cases, up to the first order of the approximation used, and it agrees with the results obtained by Allcock & Erdélyi (2017).

4. Conclusions

A mathematical model of a magnetized plasma slab sandwiched between an arbitrary number of plasma interfaces is considered, generalizing MHD wave studies in a plasma slab embedded in an asymmetric environment studied by Allcock & Erdélyi (2017, 2018). It was shown that, unlike the symmetric case investigated by Roberts (1981b), the dispersion relation does not decouple into dispersion relations of independent modes, resulting now in the existence of solutions with mixed properties, namely the quasi-kink and quasi-sausage modes.

Analytical solutions for the two- and three-slab cases were obtained in the incompressible limit. It is worth noting that the overall behavior of the phase speed of the modes (i.e., the dispersion) for multilayered slabs is similar to that of the asymmetric single slab case. The phase speeds approach either the Alfvén speed or zero in the thin-slab limit, and they converge to different speeds in the wide slab limit.

Next, the thin-slab approximation for surface waves was investigated. It is noted that, up to first order in kx_0, the solutions depend on the equilibrium parameters only of the magnetic slab and the plasma environment at infinity. Furthermore, for both cases $d_1^L \approx d_1^R \approx d_0 \ll \lambda$ and $d_1^L \approx d_1^R \ll d_0 \ll \lambda$, the solutions remain the same.

There is potential applicability as an SMS diagnostic tool of our current model put forward. We have illustrated that the spatial distribution of the oscillation amplitudes depend on the type of structuring of the equilibrium model. We have also shown that in asymmetric (multi-)slab configurations, the oscillation amplitudes are different at the boundaries of these slabs. Since these amplitude ratios are observable, assuming adequate instrumental resolution is available, knowing them and some other parameters such as the wave frequency, wavelength, or magnetic and nonmagnetic slab widths, further equilibrium parameters of the MHD waveguide could be diagnosed and determined. The property of the oscillation amplitude ratio is proposed to be seen as a novel diagnostic tool to unveil the approximate structuring of local solar multilayered MHD waveguides, analogous to Allcock & Erdélyi (2018) for a single asymmetric waveguide. Furthermore, there is another distinct property of the oscillations in asymmetric slab equilibria that could be exploited for SMS: namely the discontinuity in the derivatives in the (velocity) perturbation as shown here (or for other eigenfunctions, like magnetic field, etc.) could be exploited for indication of the actual structuring present that should be taken into account when modeling the wave propagation in such media. Such discontinuities may be deduced from suitable time–distance plots of a given oscillating asymmetric MHD waveguide, yielding further evidence about its structuring.

A direct application of the considered model might be the analysis of wave propagation in elongated MBPs of the solar photosphere. Knowing the characteristic parameters of neighboring granular cells, one would be able to find out what is the least amount of granular cells that one should consider for a correct description of waves in MBPs. With the completion of the next generation of solar telescopes with ultra-high resolution, e.g., the Daniel K. Inouye Solar Telescope (DKIST), significant improvement is expected in studying wave phenomena in MBPs; therefore, the ability to better address the wave coupling between the solar photosphere and the lower solar atmosphere above it will be enabled. Further applications to the MHD wave diagnostics of sunspot light bridges, light walls, or the oscillations in the filamentary structure of sunspot penumbrae.

The authors are grateful to M.S. Ruderman for a number of fruitful discussions and to M. Allcock for proofreading the article. D.S. acknowledges support from the University of Sheffield. R.E. is grateful to Science and Technology Facilities Council (STFC grant No. ST/M000826/1) UK for the support received.

Appendix A
Boundary Conditions in Matrix Form

It is possible to rewrite the boundary conditions (13) in matrix form (14), where $\boldsymbol{M}$ has dimension $[4 + 2(p + q)] \times [4 + 2(n + q)]$. The precise form of the matrix, with the first row corresponding to the continuity of the velocity at $x = -x_p^L$, is:

$$\begin{aligned} &\boldsymbol{M}[1, 1] = \cosh m_{p+1}^L x_p^L - \sinh m_{p+1}^L x_n^L, \\ &\boldsymbol{M}[1, 2] = -\cosh m_p^L x_p^L, \quad \boldsymbol{M}[1, 3] = \sinh m_p^L x_p^L. \end{aligned} \tag{33}$$

The second row represents the continuity of the total pressure at $x = -x_p^L$:

$$\begin{aligned} &\boldsymbol{M}[2, 1] = \Lambda_{p+1}^L(\cosh m_{p+1}^L x_p^L - \sinh m_{p+1}^L x_p^L) \\ &\boldsymbol{M}[2, 2] = \Lambda_n^L \sinh m_p^L x_p^L, \quad \boldsymbol{M}[2, 3] = -\Lambda_p^L \cosh m_p^L x_p^L. \end{aligned} \tag{34}$$

The penultimate row corresponds to the continuity of the velocity at $x = x_q^R$:

$$\begin{aligned}
\boldsymbol{M}[2(p+q)+3,\,2(p+q)+2] &= \cosh m_q^R x_q^R,\\
\boldsymbol{M}[2(p+q)+3,\,2(p+q)+3] &= \sinh m_q^R x_q^R,\\
\boldsymbol{M}[2(p+q)+3,\,2(p+q)+4] &= \sinh m_{q+1}^R x_q^R\\
&\quad - \cosh m_{q+1}^R x_q^R. \qquad (35)
\end{aligned}$$

Finally, the last row that represents the continuity of the total pressure at $x = x_q^R$, and is:

$$\begin{aligned}
\boldsymbol{M}[2(p+q)+4,\,2(p+q)+2] &= \Lambda_q^R \sinh m_q^R x_q^R,\\
\boldsymbol{M}[2(p+q)+4,\,2(p+q)+3] &= \Lambda_q^R \cosh m_q^R x_q^R,\\
\boldsymbol{M}[2(p+q)+4,\,2(p+q)+4] &= \Lambda_{q+1}^R(\cosh m_{q+1}^R x_q^R\\
&\quad - \sinh m_{q+1}^R x_q^R). \qquad (36)
\end{aligned}$$

For $1 \leqslant i \leqslant p$, the general boundary condition on the left regions takes the form

$$\begin{aligned}
\boldsymbol{M}[2i+1,\,2i] &= \cosh m_{p-i+1}^L x_{(p-i)}^L,\\
\boldsymbol{M}[2i+1,\,2i+1] &= -\sinh m_{p-i+1}^L x_{(p-i)}^L,\\
\boldsymbol{M}[2i+1,\,2i+2] &= -\cosh m_{p-i}^L x_{(p-i)}^L,\\
\boldsymbol{M}[2i+1,\,2i+3] &= \sinh m_{p-i}^L x_{(p-i)}^L,\\
\boldsymbol{M}[2i+2,\,2i] &= -\Lambda_{p-i+1}^L \sinh m_{p-i+1}^L x_{(p-i)}^L,\\
\boldsymbol{M}[2i+2,\,2i+1] &= \Lambda_{p-i+1}^L \cosh m_{p-i+1}^L x_{(p-i)}^L,\\
\boldsymbol{M}[2i+2,\,2i+2] &= \Lambda_{p-i}^L \sinh m_{p-i}^L x_{(p-i)}^L,\\
\boldsymbol{M}[2i+2,\,2i+3] &= -\Lambda_{p-i}^L \cosh m_{p-i}^L x_{(p-i)}^L. \qquad (37)
\end{aligned}$$

For $p+1 \leqslant i \leqslant p+q$, the general boundary condition on the right regions is

$$\begin{aligned}
\boldsymbol{M}[2i+1,\,2i] &= \cosh m_{i-p-1}^R x_{(i-p-1)}^R,\\
\boldsymbol{M}[2i+1,\,2i+1] &= \sinh m_{i-p-1}^R x_{(i-p-1)}^R,\\
\boldsymbol{M}[2i+1,\,2i+2] &= -\cosh m_{i-p}^R x_{(i-p-1)}^R,\\
\boldsymbol{M}[2i+1,\,2i+3] &= -\sinh m_{i-p}^R x_{(i-p-1)}^R,\\
\boldsymbol{M}[2i+2,\,2i] &= \Lambda_{i-p-1}^R \sinh m_{i-p-1}^R x_{(i-p-1)}^R,\\
\boldsymbol{M}[2i+2,\,2i+1] &= \Lambda_{i-p-1}^R \cosh m_{i-p-1}^R x_{(i-p-1)}^R,\\
\boldsymbol{M}[2i+2,\,2i+2] &= -\Lambda_{i-p}^R \sinh m_{i-p}^R x_{(i-p-1)}^R,\\
\boldsymbol{M}[2i+2,\,2i+3] &= -\Lambda_{i-p}^R \cosh m_{i-p}^R x_{(i-p-1)}^R. \qquad (38)
\end{aligned}$$

For the rest of the values, $\boldsymbol{M}[i, j] = 0$.

Appendix B
Dispersion Relation for Thin-slab Approximation

1.1 Two-slab Case

Let us now derive the dispersion relation, up to first order in kx_0, under the thin-slab approximation. From Equation (18), we found a power series expansion with respect to x_0 and d_1^L, namely,

$$\begin{aligned}
&\rho_0\left(\frac{m_1^R}{\rho_1^R} + \frac{m_2^L}{\rho_2^L}\right)\omega^2(\omega^2 - k^2 v_A^2)\\
&\quad + 2x_0\left(m_0^2\omega^4 + \frac{m_1^R m_2^L}{\rho_1^R \rho_2^L}\rho_0^2(\omega^2 - k^2 v_A^2)^2\right)\\
&\quad + d_1^L \rho_0\left(\frac{m_1^L m_1^L}{\rho_1^L} + \frac{m_1^R m_2^L \rho_1^L}{\rho_1^R \rho_2^L}\right)\omega^2(\omega^2 - k^2 v_A^2)\\
&\quad + 2x_0 d_1^L\left(\frac{m_0^2 m_2^L \rho_1^L \omega^4}{\rho_2^L} + \frac{m_1^L m_1^L m_1^R \rho_0^2(\omega^2 - k^2 v_A^2)^2}{\rho_1^L \rho_1^R}\right)\\
&\quad + O[x_0]^3 + O[d_1^L]^3 = 0. \qquad (39)
\end{aligned}$$

If $d_1^L \ll d_0 \ll \lambda$, up to the first order in kx_0, using Equation (39), we have

$$\begin{aligned}
&\rho_0\left(\frac{m_1^R}{\rho_1^R} + \frac{m_2^L}{\rho_2^L}\right)\omega^2(\omega^2 - k^2 v_A^2)\\
&\quad + 2x_0\left(m_0^2\omega^4 + \frac{m_1^R m_2^L}{\rho_1^R \rho_2^L}\rho_0^2(\omega^2 - k^2 v_A^2)^2\right) = 0. \qquad (40)
\end{aligned}$$

If $d_1^L \approx d_0 \ll \lambda$, again, up to the first order of approximation in kx_0, from Equation (39), we obtain

$$\begin{aligned}
&\rho_0\left(\frac{m_1^R}{\rho_1^R} + \frac{m_2^L}{\rho_2^L}\right)\omega^2(\omega^2 - k^2 v_A^2)\\
&\quad + 2x_0\left(m_0^2\omega^4 + \frac{m_1^R m_2^L}{\rho_1^R \rho_2^L}\rho_0^2(\omega^2 - k^2 v_A^2)^2\right)\\
&\quad + d_1^L \rho_0\left(\frac{m_1^L m_1^L}{\rho_1^L} + \frac{m_1^R m_2^L \rho_1^L}{\rho_1^R \rho_2^L}\right)\omega^2(\omega^2 - k^2 v_A^2) = 0. \qquad (41)
\end{aligned}$$

1.2 Three-slab Case

For Equation (20), we obtain a power series expansions in kx_0, with respect to x_0, d_1^L, and d_1^R:

$$\begin{aligned}
&\rho_0(m_2^R\rho_2^L + m_2^L\rho_2^R)\omega^2(\omega^2 - k^2v_A^2)\\
&\quad + 2x_0(m_0^2\omega^4\rho_2^L\rho_2^R + m_2^Lm_2^R\rho_0^2(\omega^2 - k^2v_A^2)^2)\\
&\quad + d_1^R\frac{\rho_0}{\rho_1^R}(m_2^Lm_2^R\rho_1^R\rho_1^R + m_1^Rm_1^R\rho_2^L\rho_2^R)\omega^2(\omega^2 - k^2v_A^2)\\
&\quad + d_1^L\frac{\rho_0}{\rho_1^L}(m_2^Lm_2^R\rho_1^L\rho_1^L + m_1^Lm_1^L\rho_2^L\rho_2^R)\omega^2(\omega^2 - k^2v_A^2)\\
&\quad + 2x_0\frac{d_1^R}{\rho_1^R}[m_0^2m_2^R\rho_1^R\rho_1^R\rho_2^L\omega^4\\
&\quad + m_1^Rm_1^Rm_2^L\rho_0^2\rho_2^R(\omega^2 - k^2v_A^2)^2]\\
&\quad + 2x_0\frac{d_1^L}{\rho_1^L}[m_0^2m_2^L\rho_1^L\rho_1^L\rho_2^R\omega^4\\
&\quad + m_1^Lm_1^Lm_2^R\rho_0^2\rho_2^L(\omega^2 - k^2v_A^2)^2]\\
&\quad + \frac{d_1^Rd_1^L}{\rho_1^L\rho_1^R}[\rho_0(m_1^Lm_1^Lm_2^R\rho_1^R\rho_1^R\rho_2^L + m_1^Rm_1^Rm_2^L\rho_1^L\rho_1^L\rho_2^R)\\
&\quad \times \omega^2(\omega^2 - k^2v_A^2)] + O[x_0]^3 + O[d_1^R]^3 + O[d_1^L]^3 = 0.
\end{aligned} \tag{42}$$

If $d_1^L \approx d_1^R \ll d_0 \ll \lambda$, up to first order in kx_0, from Equation (42), we acquire

$$\begin{aligned}
&\rho_0(m_2^R\rho_2^L + m_2^L\rho_2^R)\omega^2(\omega^2 - k^2v_A^2)\\
&\quad + 2x_0(m_0^2\omega^4\rho_2^L\rho_2^R + m_2^Lm_2^R\rho_0^2(\omega^2 - k^2v_A^2)^2) = 0.
\end{aligned} \tag{43}$$

If $d_1^L \approx d_1^R \approx d_0 \ll \lambda$, from Equation (42), we have

$$\begin{aligned}
&\rho_0(m_2^R\rho_2^L + m_2^L\rho_2^R)\omega^2(\omega^2 - k^2v_A^2)\\
&\quad + 2x_0(m_0^2\omega^4\rho_2^L\rho_2^R + m_2^Lm_2^R\rho_0^2(\omega^2 - k^2v_A^2)^2)\\
&\quad + d_1^R\frac{\rho_0}{\rho_1^R}(m_2^Lm_2^R\rho_1^R\rho_1^R + m_1^Rm_1^R\rho_2^L\rho_2^R)\omega^2(\omega^2 - k^2v_A^2)\\
&\quad + d_1^L\frac{\rho_0}{\rho_1^L}(m_2^Lm_2^R\rho_1^L\rho_1^L + m_1^Lm_1^L\rho_2^L\rho_2^R)\omega^2(\omega^2 - k^2v_A^2) = 0
\end{aligned} \tag{44}$$

ORCID iDs

Daria Shukhobodskaia https://orcid.org/0000-0001-5302-6253
Róbert Erdélyi https://orcid.org/0000-0003-3439-4127

References

Abbo, L., Ofman, L., Antiochos, S. K., et al. 2016, SSR, 201, 55
Alfvén, H. 1947, MNRAS, 107, 211
Allcock, M., & Erdélyi, R. 2017, SoPh, 292, 35
Allcock, M., & Erdélyi, R. 2018, ApJ, 855, 90
Andries, J., Van Doorsselaere, T., Roberts, B., et al. 2009, SSR, 149, 3
Arregui, I., Oliver, R., & Ballester, J. L. 2012, LRSP, 9, 2
Aschwanden, M. 2005, Physics of the Solar Corona (Berlin: Springer)
Banerjee, D., Erdélyi, R., Oliver, R., & O'Shea, E. 2007, SoPh, 246, 3
Belcher, J. W. 1971, ApJ, 168, 509
De Moortel, I. 2009, SSR, 149, 65
DeForest, C. E., & Gurman, J. B. 1998, ApJ, 501, 217
Edwin, P. M., & Roberts, B. 1982, SoPh, 76, 239
Erdélyi, R. 2006a, RSPTA, 364, 289
Erdélyi, R. 2006b, in Proc. SOHO 18/GONG 2006/HELAS I, Beyond the Spherical Sun, ESA SP-624, ed. K. Fletcher & M. Thompson (Noordwijk: ESA), 15
Erdélyi, R., & Taroyan, Y. 2008, A&A, 489, L49
Goossens, M., Erdélyi, R., & Ruderman, M. S. 2011, SSRv, 158, 289
Hollweg, J. V. 1991, in Mechanisms of Chromospheric and Coronal Heating, ed. P. Ulmschneider, E. R. Priest, & R. Rosner (Berlin: Springer), 423
Ionson, J. A. 1978, ApJ, 226, 650
Liu, Y., Xiang, Y., Erdélyi, R., et al. 2018, ApJ, in press
Mathioudakis, M., Jess, D. B., & Erdélyi, R. 2013, SSRv, 175, 1
Nakariakov, V. M. 2006, RSPTA, 364, 473
Nakariakov, V. M., & Ofman, L. 2001, A&A, 372, L53
Nakariakov, V. M., & Verwichte, E. 2005, LRSP, 2, 3
Ofman, L., Romoli, M., Poletto, G., et al. 1997, ApJL, 491, L111
Osterbrock, D. E. 1961, ApJ, 134, 347
Roberts, B. 1981a, SoPh, 69, 27
Roberts, B. 1981b, SoPh, 69, 39
Roberts, B. 2000, SoPh, 193, 139
Roberts, B., Edwin, P. M., & Benz, A. O. 1984, ApJ, 279, 857
Ruderman, M. S. 1992, JGR, 97, 16
Ruderman, M. S., & Erdélyi, R. 2009, SSR, 149, 199
Tandberg-Hanssen, E. 1995, The Nature of Solar Prominences (Dordrecht: Kluwer)
Thompson, B. J., Plunkett, S. P., Gurman, J. B., et al. 1998, GeoRL, 25, 2465
Tsiropoula, G., Tziotziou, K., Kontogiannis, I., et al. 2012, SSR, 169, 181
Uchida, Y. 1970, PASJ, 22, 341
Wang, T. J. 2004, in Waves, Oscillations and Small Scale Transient Events in the Solar Atmosphere: A Joint View of SOHO and TRACE, ESA-SP 547, ed. R. Erdélyi et al. (Noordwijk: ESA), 417
Yang, S., Zhang, J., & Erdélyi, R. 2016, ApJL, 833, L18
Yang, S., Zhang, J., Erdélyi, R., et al. 2017, ApJL, 843, L15
Yuan, D., Nakariakov, V. M., Huang, Z., et al. 2014, ApJ, 792, 1
Zaitsev, V. V., & Stepanov, A. V. 1975, IGAFS, 37, 3
Zaqarashvili, T. V., & Erdélyi, R. 2009, SSRv, 149, 355
Zsámberger, N. K., Allcock, M., & Erdélyi, R. 2018, ApJ, 853, 136